Volume 18 | Number 12 | 28 March 2016 | Pages 2027–2212

CrystEngComm

www.rsc.org/crystengcomm

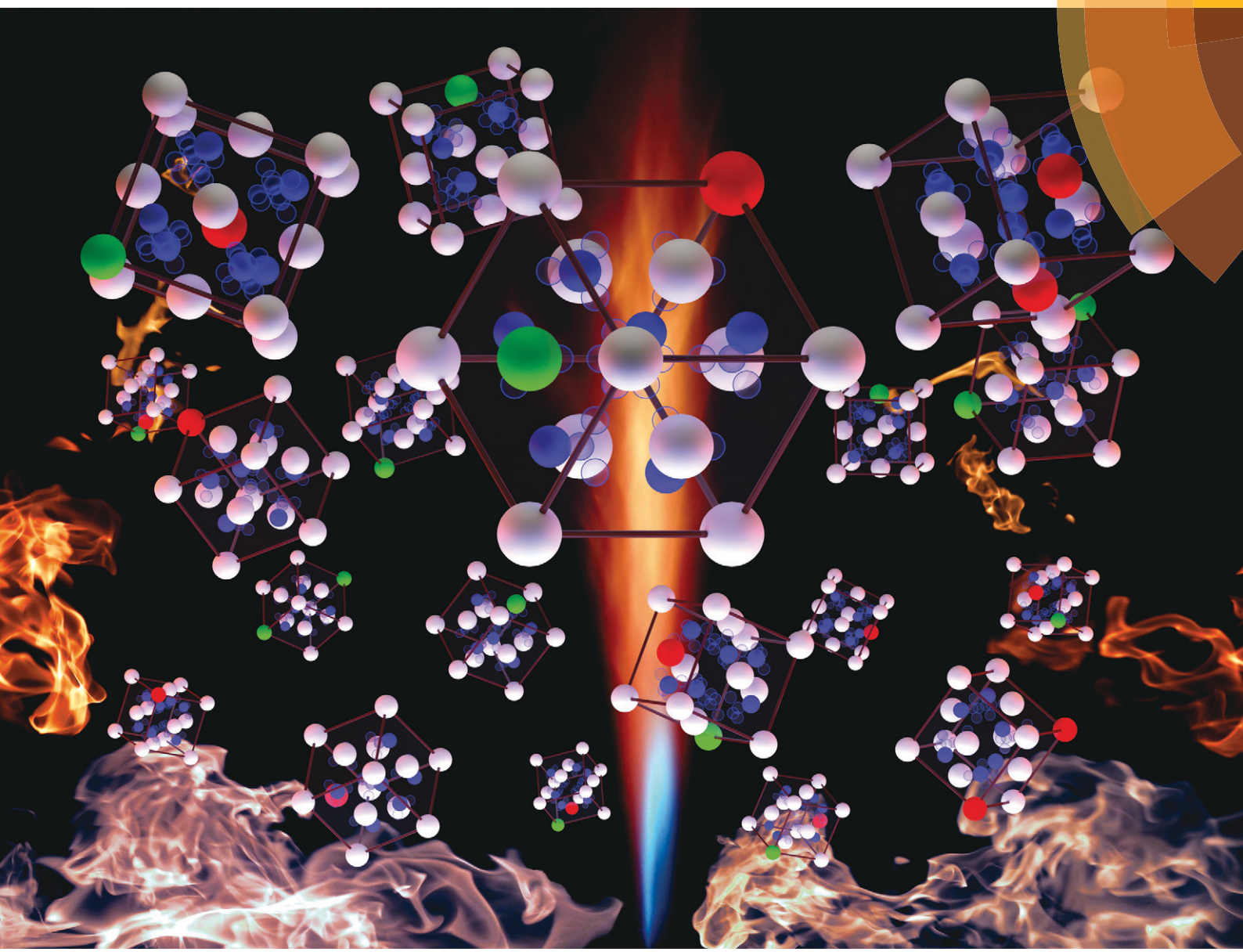

ROYAL SOCIETY OF CHEMISTRY

PAPER

Lutz Mädler *et al.*

Decrease of the required dopant concentration for δ-Bi_2O_3 crystal stabilization through thermal quenching during single-step flame spray pyrolysis

175 YEARS

CrystEngComm

PAPER

View Article Online
View Journal | View Issue

Cite this: *CrystEngComm*, 2016, **18**, 2046

Decrease of the required dopant concentration for δ-Bi_2O_3 crystal stabilization through thermal quenching during single-step flame spray pyrolysis†

Jochen A. H. Dreyer,[a] Suman Pokhrel,[b] Johannes Birkenstock,[c] Miguel G. Hevia,[d] Marco Schowalter,[e] Andreas Rosenauer,[e] Atsushi Urakawa,[d] Wey Yang Teoh[a] and Lutz Mädler*[b]

Received 11th December 2015,
Accepted 28th January 2016

DOI: 10.1039/c5ce02430g

www.rsc.org/crystengcomm

δ-Bi_2O_3 is one of the best oxygen ion conductors known. However, due to its limited thermal stability and complicated synthesis techniques, its applications are limited. Here, the synthesis of stable nano-sized δ-Bi_2O_3 using versatile and rapid flame spray pyrolysis (FSP) combined with *in situ* Ti and/or Mn doping for an enhanced thermal stability is reported for the first time. Exceptionally low Bi replacing cation concentrations (8 at% Ti) were sufficient to obtain phase-pure δ-Bi_2O_3 which was attributed to the extraordinarily high temperature gradient during FSP. The required cation amount for δ-phase stabilization was even further reduced by introducing mixtures of Mn and Ti (2.5 at% Mn + 2.5 at% Ti). Rietveld analysis revealed that the δ-Bi_2O_3 structure is best represented by the $Fm\bar{3}m$ space group containing two closely neighbored 8*c* and 32*f* Wyckoff positions. Depending on the amount of Mn/Ti cations, about 25% of the possible oxygen positions remain vacant, suggesting high bulk oxygen mobility. The enhanced oxygen mobility was confirmed by temperature programmed reduction (H_2-TPR) with bulk reduction for δ-Bi_2O_3 in contrast to exclusive surface reduction for β-Bi_2O_3.

Introduction

Tuning the crystal structure of polymorphic metal oxides can yield materials with unique properties such as TiO_2 with a modified anatase/rutile ratio for improved photocatalysis[1,2] or cubic ZrO_2 stabilized by Y^{3+} for solid oxide fuel cells (SOFCs).[3] A polymorphic material that gained increasing attention is Bi_2O_3 as its high-temperature δ-phase exhibits the highest oxygen ion conductivity among the known oxide ceramics.[4–6] Ion conductivity in solid oxides originates from the hopping of oxygen ions within the crystal structure to adjacent equivalent but vacant oxygen sites.[7,8] The reason for the extraordinarily high oxygen mobility in δ-Bi_2O_3 was attributed to the high number of oxygen vacancies the δ-phase naturally possesses.[9,10] However, cubic δ-Bi_2O_3 is only thermodynamically stable at 729–824 °C,[9,10] while the metastable β- or γ-Bi_2O_3 and stable α-Bi_2O_3 phases are formed during the cooling,[6,11] significantly complicating the synthesis of δ-Bi_2O_3 and limiting its use in different applications. Numerous attempts were made to extend the low-temperature stability of δ-Bi_2O_3 such as electrodeposition on single and polycrystalline Au as well as on stainless steel substrates.[10,12] Reactive sputtering[13] and chemical vapor deposition[14] are also known to be suitable techniques for obtaining pure thin-film δ-Bi_2O_3. Another approach for stabilizing δ-Bi_2O_3 at lower temperatures is through the formation of solid solutions by partially replacing Bi with other cations.[15–18] The most commonly used cations (referred to as dopants in spite of the high concentrations) for this purpose are the lanthanides, yttrium and a few other transition metals.[9,15,19] However, admixing foreign metal ions potentially lowers the cation polarizability of δ-Bi_2O_3, and as such, low dopant concentrations are desirable for stabilizing δ-Bi_2O_3.[16] Co-doping with more than one cation was shown to reduce the required amount of dopants due to the increased

[a] *Clean Energy and Nanotechnology (CLEAN) Laboratory, School of Energy and Environment, City University of Hong Kong, Hong Kong SAR*
[b] *Foundation Institute of Materials Science (IWT), Department of Production Engineering, University of Bremen, Germany. E-mail: lmaedler@iwt.uni-bremen.de*
[c] *Central Laboratory for Crystallography and Applied Materials, University of Bremen, Germany*
[d] *Institute of Chemical Research of Catalonia (ICIQ), Tarragona, Spain*
[e] *Institute of Solid State Physics, University of Bremen, Germany*

† Electronic supplementary information (ESI) available: EELS spectra of the $L_{2,3}$ edge of Mn or Ti for selected δ-Bi_2O_3 samples and corresponding L_2/L_3 peak fitting for determining the Mn oxidation state; ion currents of m/z = 44 (CO_2) for the H_2-TPR experiments presented in Fig. 9. See DOI: 10.1039/c5ce02430g

structural and mixing entropies.[16,20] To date, however, the required amount of dopants is commonly larger than 12 at%, while requiring costly and time-consuming processing such as solid-state reactions and wet chemical routes.[5,15–17,20,21]

Here, we introduce the rapid synthesis of δ-Bi_2O_3 nanoparticles using flame spray pyrolysis (FSP). The FSP method is an elegant and industrially relevant single-step technique for the synthesis of nanosized metal oxides.[22] The extraordinarily high quenching rates associated with the flame synthesis resulted in many metastable phases with precisely controlled composition of both the dopants and the host matrix.[23,24] The rapid quenching nature of the FSP method affords exceptionally low concentrations of Ti and/or Mn dopants to yield δ-phase Bi_2O_3 stable at room temperature.

Experimental section

Material preparation

A single-nozzle flame spray pyrolysis (FSP)[22] method was utilized for the synthesis of Ti- and Mn-doped Bi_2O_3 particles. The required amounts of titanium(IV) isopropoxide (97%; Aldrich), bismuth neodecanoate (Aldrich), and manganese(II) 2-ethylhexanoate (40% in mineral spirits; Strem Chemicals) were dissolved in xylene (≥99.5%; Aldrich) for an overall metal concentration of 0.5 M (see Table 1). Subsequently, 5 mL min^{-1} precursor solution was fed to the nozzle with a syringe pump, dispersed into fine droplets by 5 L min^{-1} O_2, and inflamed by a 1.5 L min^{-1} CH_4/3.2 L min^{-1} O_2 supporting flame. The pressure drop at the nozzle tip was kept constant at 1.5 bar. The particles were collected on GF/D (Whatman) glass fiber filters of 25.7 cm diameter, from which they were recovered for further analyses. A MnO_x reference sample was synthesized for UV/vis analyses with identical flame parameters and a 0.5 M solution of manganese(II) 2-ethylhexanoate (40% in mineral spirits; Strem Chemicals) in xylene.

Instruments and characterization

Transmission electron microscopy (TEM) was carried out using a FEI Titan 80/300 ST electron microscope equipped with a corrector for spherical aberration of the objective lens and a Gatan imaging filter (GIF) for electron energy loss spectroscopy (EELS). Samples for TEM were prepared by dispersing the particles in acetone and dripping the solution on Cu grids covered with a thin amorphous carbon film. The Bi_2O_3 particle size was determined from TEM by measuring at least 100 particles per sample. The Mn oxidation state was determined using an EELS method reported by Cavé *et al.*[25] A power law background was fitted to a region before the Mn $L_{2,3}$ edge and then subtracted from the signal yielding the Mn $L_{2,3}$ edge (ESI,† Fig. S1). The double arctan background was fitted to the Mn $L_{2,3}$ edge and the intensity between the background in the L_2 and the L_3 peak was integrated within 4 eV windows. Room temperature XRD patterns were measured using a Philips PW1800 diffractometer equipped with Cu K_α radiation produced at 40 kV and 30 mA. A secondary monochromator with a classical point detector and an automatic divergence slit fixing the beam spot on the sample to a length of 2 mm was used. High-temperature XRD measurements were performed using a PANalytical X'Pert MPD Pro diffractometer equipped with secondarily Ni-filtered Cu K_α radiation (45 kV and 40 mA), an Anton Paar HTK1200N heating chamber and an X'Celerator detector. The binding energies were measured with X-ray photoelectron spectroscopy (XPS, Physical Electronics, PHI-5802) equipped with a monochromated Al K_α X-ray source at 11.75 eV pass energy and were referenced with the C 1s peak at 284.7 eV. H_2 temperature programmed reduction (H_2-TPR) was measured with an AutoChem 2950 HP Chemisorption Analyzer (Micromeritics) and connected MicroStar Mass Spectrometer (Micromeritics). About 20 mg of as-synthesized sample were placed in a quartz tube, cooled to 0 °C under Ar flow with the aid of a CryoCooler (Micromeritics), and heated to 600 °C at 10 °C min^{-1} under 50 mL min^{-1} of 5% H_2/Ar flow.

Temporal analysis of products

The temporal analysis of products (TAP) was measured with a TAP-2 reactor (Mithra Technologies, Inc.). The powder samples were pressed at 180 kg cm^{-2}, ground and sieved to a fraction of 125–400 μm. From the as-prepared pellets 100 mg were placed in a quartz reactor (inner diameter 3.8 mm)

Table 1 The sample composition, BET specific surface areas (SSA), primary particle diameter (d_{BET}), crystal phases, and the optical bandgap (E_g) of pristine and doped Bi_2O_3 samples as-prepared with flame spray pyrolysis

Sample	Mn at%	Ti at%	Bi at%	SSA m^2 g^{-1}	d_{BET} nm	Major crystal phase	E_g eV
β-Bi_2O_3	0	0	100	32	20[a]	β	2.3
2%Ti–Bi_2O_3	0	2	98	41	16[b]	β + δ	2.4
4%Ti–Bi_2O_3	0	4	96	45	15[b]	β + δ	2.6
5%Ti–Bi_2O_3	0	5	95	—	—	β + δ	2.6
6%Ti–Bi_2O_3	0	6	94	49	14[b]	β + δ	2.7
8%Ti–Bi_2O_3	0	8	92	50	13[b]	δ	2.7
10%Ti–Bi_2O_3	0	10	90	45	15[a]	δ	2.8
5%Mn–Bi_2O_3	5	0	95	46	15[b]	β	—
10%Mn–Bi_2O_3	10	0	90	45	16[a]	δ	1.9
1%Mn–1%Ti–Bi_2O_3	1	1	98	—	—	β + δ	—
2.5%Mn–2.5%Ti–Bi_2O_3	2.5	2.5	95	44	15[a]	δ	—
5%Mn–5%Ti–Bi_2O_3	5	5	90	46	15[a]	δ	1.6

Values were calculated assuming spherical particles. [a] Densities determined using Rietveld analysis. [b] Theoretically calculated densities.

between two layers of quartz beads with 125–200 μm diameter. A thermocouple inside the catalyst zone was used for the temperature control. Prior to the experiments the samples were pretreated with 20 mL min^{-1} He at 250 °C for 1 h, after which the reactor was evacuated (<8 × 10^{-8} torr). Small and ultrashort pulses of 66.7% $^{18}O_2$ in Ar were exposed to the sample while the reactor outlet gases were monitored using a mass spectrometer (m/z = 40, 32, 34, and 36 for Ar, $^{16}O_2$, $^{16}O^{18}O$, and $^{18}O_2$, respectively). The Knudsen diffusion regime was validated by varying the O_2/Ar pulse size and fitting the Ar signal to the dimensionless exit flow $\bar{F}_A$ based on the dimensionless diffusion equation:[26]

$$\bar{F}_A = -\frac{\partial \bar{C}_A}{\partial \xi} \quad (1)$$

$$\frac{\partial \bar{C}_A}{\partial \tau} = \frac{\partial^2 \bar{C}_A}{\partial \xi^2} \quad (2)$$

Initial and boundary conditions:

$$\bar{C}_A(\xi, 0) = \delta_\xi \quad (3)$$

$$\frac{\partial \bar{C}_A(0,\tau)}{\partial \xi} = 0 \quad (4)$$

$$\bar{C}_A(1,\tau) = 0 \quad (5)$$

with $\bar{C}_A$ and ξ being the dimensionless concentration and axial coordinate, respectively, and the delta function δ_ξ. The dimensionless time τ is defined as:[26]

$$\tau = \frac{t \cdot D_{eA}}{\varepsilon_b \cdot L^2} \quad (6)$$

with the time t, effective Knudsen diffusivity D_{eA}, fractional voidage of the reactor bed ε_b and reactor length L. Within the catalyst zone, gas adsorption and desorption was considered using the reversible adsorption equation:[26]

$$\frac{\partial \bar{C}_A}{\partial_\tau} = \frac{\partial^2 \bar{C}_A}{\partial \xi^2} - \frac{\partial \bar{\theta}_A}{\partial \tau} = \frac{\partial^2 \bar{C}_A}{\partial \xi^2} - \bar{k}_a \bar{C}_A + \bar{k}_d \bar{\theta}_A \quad (7)$$

with the dimensionless surface coverage $\bar{\theta}_A$ and the adsorption and desorption rate constants $\bar{k}_a$ and $\bar{k}_d$. Eqn (2) and (7) were converted to ordinary differential equations by the method of lines and solved with the initial and boundary conditions (3)–(5) with the ode15s solver in Matlab. The constants $D_{eA} \cdot \varepsilon_b^{-1} \cdot L^{-2}$ in eqn (6) and $\bar{k}_a$ and $\bar{k}_d$ in eqn (7) were determined by varying their value independently until the best fit between the solution of eqn (1) and the experimental peak shape was achieved. Experiments without any catalyst (*i.e.*, only with quartz beads) were conducted to quantify the Ar to $^{18}O_2$ peak area ratio for 100% O_2 exiting the reactor (*i.e.*, no O_2 consumed; referred to as "Inlet O_2" in the manuscript) and was used to identify possible consumptions of oxygen during the experiments.

Results and discussion

Particle morphology and structural characterization

Flame spray pyrolysis (FSP) of the organometallic precursor consisting of bismuth neodecanoate in xylene resulted in tetragonal β-Bi_2O_3 as shown from the XRD pattern and Rietveld analysis in Fig. 1a. This is consistent with an earlier work using dissolved bismuth nitrate in acetic acid as the liquid precursor.[27] As mentioned earlier, β-Bi_2O_3 is a metastable phase formed during the cooling from high temperatures.[6] In the case of xylene-based precursor, the flame temperature could be as high as 2130 °C at the ignition point before being rapidly quenched at approximately 170 °C cm^{-1} within the flame to ~800 °C at the tip of the flame.[24] Along the flame axis, combustion of the liquid metal precursor resulted in a metal/metal oxide vapor that was quickly followed by the

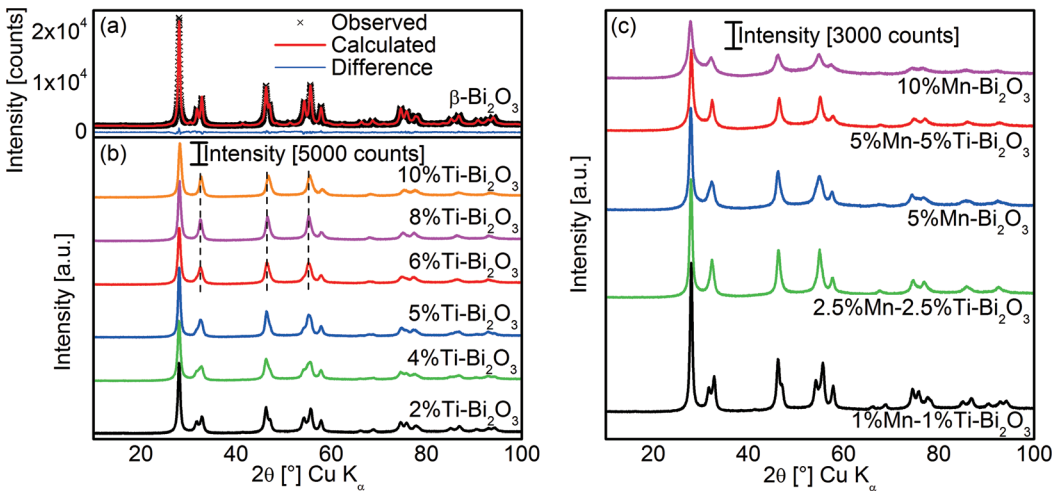

Fig. 1 (a) The Rietveld refinement fit of the XRD pattern of flame-prepared pristine β-Bi_2O_3 and (b) the corresponding patterns with increasing amounts of Ti dopant. (c) The XRD patterns of flame-prepared Bi_2O_3 doped with different amounts of Mn and that co-doped with Ti.

sequential aerosol particle formation processes of nucleation, coalescence, aggregation and agglomeration.[28]

The doping of Bi_2O_3 was carried out by co-dissolving titanium isopropoxide and/or manganese 2-ethylhexanoate in the original precursor formulation. As shown in Fig. 1b, the doping of Ti resulted in the gradual transformation of β-Bi_2O_3 to δ-Bi_2O_3 as evident from the merging of diffraction peaks at 32°, 46.5°, 55° and 75°. Essentially, pure δ-Bi_2O_3 was obtained at 8 at% Ti. Here, the doping of Ti stabilized the δ-Bi_2O_3 phase during rapid flame particle formation and suppressed the transformation to β-Bi_2O_3 during the cooling process. A further increase to 10 at% Ti shifted the diffraction peaks towards higher Bragg angles as a result of the shrinkage in lattice parameters from the substitutional replacement of hexacoordinated Bi^{3+} (ionic radius 0.103 nm)[29] with the smaller Ti^{4+} ions (ionic radius 0.0605 nm; see XPS below for Ti oxidation state).[29] Depending on the preparation conditions and Ti content, other reports on techniques without rapid quenching/cooling resulted in ternary phases such as $Bi_{12}TiO_{20}$, and $Bi_4Ti_3O_{12}$ or β-Bi_2O_3.[30,31] In the case of FSP, the small amount of Ti coupled with the short residence time in the flame prevented the crystallization of ternary oxides. More importantly, the combination of doping and rapid quenching resulted in room temperature stable δ-Bi_2O_3 phase.

The studies of *in situ* flame doping were extended to that of a lower valency dopant, namely Mn^{2+}. As shown in Fig. 1c, the doping with 5 at% Mn resulted in the mixture of β- and δ-Bi_2O_3, while at 10 at% dopant, the latter structure was fully preserved. As a result of the similar ionic radii of hexacoordinated Bi^{3+} (0.103 nm)[29] and Mn^{2+} (0.083 or 0.067 nm for high and low spins, respectively; see below, EELS and XPS discussion on Mn valency)[29] no changes in the XRD peak positions were observed. With the aim of achieving even lower amounts of dopant, the synergetic effect of Ti^{4+}–Mn^{2+} co-doping was explored. At 1 at% Ti and 1 at% Mn, the δ-Bi_2O_3 phase was only partially stabilized, but with increasing equimolar dopant concentrations to 2.5 and 5 at%, full preservation of δ-Bi_2O_3 was achieved (Fig. 1c). The synergetic effect is believed to be at least in part due to the minimization of aliovalency since the net valency of +3 was preserved (matching the Bi^{3+} in Bi_2O_3). This suppresses the alteration of the number of δ-Bi_2O_3 oxygen vacancies (*i.e.*, increase for Mn^{2+} and decrease for Ti^{4+}) that otherwise promotes crystal phase transformation.[2,32]

To gain more insights on the crystal structures of the doped δ-Bi_2O_3, Rietveld analysis of the XRD patterns was carried out with the consideration of three different δ-Bi_2O_3 models: (a) the $Pn\bar{3}m$ space group with fully occupied six-fold Wyckoff positions 6*d* (Inorganic Crystal Structure Database, ICSD 37367)[33] and two $Fm\bar{3}m$ models with (b) 6 oxygen atoms on the eight-fold Wyckoff positions 8*c* (ICSD 61647)[34] and (c) 6 oxygen atoms on two closely neighbored Wyckoff positions 8*c* and 32*f* (ICSD 98144).[35] As shown in Fig. 2a, the $Pn\bar{3}m$ symmetry could not adequately describe the flame-synthesized δ-Bi_2O_3 given the absence of δ-Bi_2O_3 [011] at 23° 2θ in the FSP-made material. The two $Fm\bar{3}m$ models encompass the same set of reflections but a better description was observed by the model with the oxygen atoms adjacent to 8*c* and 32*f* Wyckoff positions (R_{Bragg} = 2.97% and $R_{p'}$ = 9.44%; Fig. 2c) compared to the alternative model (R_{Bragg} = 5.37% and $R_{p'}$ = 12.53%; Fig. 2b). The resultant Rietveld-refinement parameters and *R*-values are listed in Table 2. The crystal structure

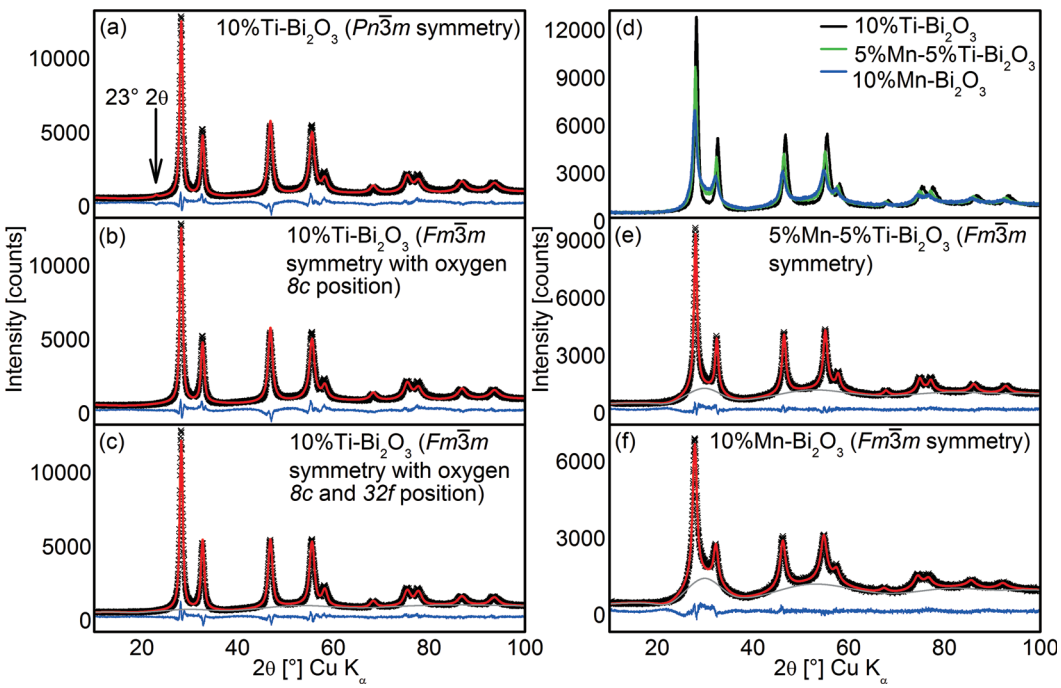

Fig. 2 The Rietveld refinement fits of the XRD pattern of 10%Ti–Bi_2O_3 using (a) the $Pn\bar{3}m$ symmetry and two $Fm\bar{3}m$ symmetries with (b) ~6 oxygen ions on the 8*c* Wyckoff positions and (c) ~6 oxygen ions on 8*c* and 32*f* Wyckoff positions. (d) Direct comparison of the overlaying XRD patterns of 10%Ti–Bi_2O_3, 5%Mn–5%Ti–Bi_2O_3 and 10%Mn–Bi_2O_3 samples. Rietveld refinement fits of the (e) 5%Mn–5%Ti–Bi_2O_3 and (f) 2.5%Mn–2.5%Ti–Bi_2O_3 samples. Measured data = black crosses, calculated pattern = red line, difference between measured and calculated pattern = blue line.

Table 2 Parameters and *R*-values obtained from Rietveld refinements for the samples with pure δ-phase

Sample	Atom	Ox	*xyz*	B_{iso}	SOF[a]	R_{Bragg}[b] %	R_{wp}[b] %	R_p[b] %	$R_{p'}$[b] %	*a* Å	Cryst. size[c] nm	Cryst. microstrain[c] %
10%Ti–Bi_2O_3	Bi1	3+	0 0 0	3.35(5)	0.01875	3.0	5.4	4.3	9.4	5.4984(6)	12(3)	2.4(2)
	Ti1	4+	0 0 0	3.35(5)	0.00208							
	O1	2−	¼ ¼ ¼	3.35(5)	0.00959							
	O2	2−	0.324(1) *x x*	3.35(5)	0.02373							
5%Mn–5%Ti–Bi_2O_3	Bi1	3+	0 0 0	3.53(6)	0.01875	2.0	4.8	3.7	11.1	5.5338(7)	10(2)	1.3(2)
	Ti1	4+	0 0 0	3.53(6)	0.00104							
	Mn1	2+	0 0 0	3.53(6)	0.00104							
	O1	2−	¼ ¼ ¼	3.53(6)	0.009							
	O2	2−	0.331(1) *x x*	3.53(6)	0.02225							
10%Mn–Bi_2O_3	Bi1	3+	0 0 0	2.8(3)	0.01875	2.0	5.2	3.8	12.5	5.563(2)	8(2)	2.4(3)
	Mn1	2+	0 0 0	2.8(3)	0.00208							
	O1	2−	¼ ¼ ¼	2.8(3)	0.0087							
	O2	2−	0.304(1) *x x*	2.8(3)	0.02151							

[a] SOF = site occupation factor. [b] $R_{Bragg} = \sum|I_o - I_c|/\sum I_o$, $R_{wp} = \sqrt{(\sum w(y_o - y_c)^2/\sum w y_o^2)}$, $R_p = \sum|y_o - y_c|/\sum y_o$, $R_{p'} = \sum|y_o - y_c|/\sum|y_o - y_b|$, with integrated intensity *I*, step intensity *y*, $w = y_o^{-0.5}$, observation o, calculation c and background b. [c] Crystallite size (*via* Scherrer equation) and microstrain calculated from phase-specific peak broadening.

reported for δ-Bi_2O_3 at 780 °C differs from the present room temperature material only in the lattice parameter and the partial replacement of Bi by Ti, affirming the successful synthesis of the high-temperature phase with the FSP process. The Rietveld analyses were extended to 5%Mn–5%Ti–Bi_2O_3 (Fig. 2e) and 10%Mn–Bi_2O_3 (Fig. 2f), showing excellent agreement between the above $Fm\bar{3}m$ model and the measured diffraction pattern (Table 2). Broad humps in the baseline of samples containing Mn dopants were traced to the aggregation of MnO_x clusters, which will be substantiated from XPS and the optical absorbance (shown below). Further to the XRD analyses, the crystallite sizes for 10%Ti–Bi_2O_3 (12 ± 3 nm), 5%Mn–5%Ti–Bi_2O_3 (10 ± 2 nm) and 10%Mn–Bi_2O_3 (8 ± 2 nm) were estimated from the Scherrer equation. These crystallite sizes were consistently smaller than the surface area-equivalent diameter of d_{BET} (Table 1), indicating the presence of sinter necks between the Bi_2O_3 crystallite particles. The estimated d_{BET} is consistent with that determined by TEM particle counting of β-Bi_2O_3 (26 ± 9 nm), 2.5%Mn–2.5%Ti–Bi_2O_3 (15 ± 5 nm), 5%Mn–5%Ti–Bi_2O_3 (15 ± 6 nm), 5%Ti–Bi_2O_3 (15 ± 6 nm) and 8%Ti–Bi_2O_3 (14 ± 5 nm) (Fig. 3). As further illustrated in Fig. 3f–o, the high-resolution TEM images show aggregates of single crystalline particles with lattice spacings belonging to the β-Bi_2O_3 (021) or δ-Bi_2O_3 (111) planes.

To analyze the details of the crystal structures of β- and δ-Bi_2O_3, their atom arrangement was studied based on the Rietveld refinement results shown in Fig. 1a and 2c. The Bi atom

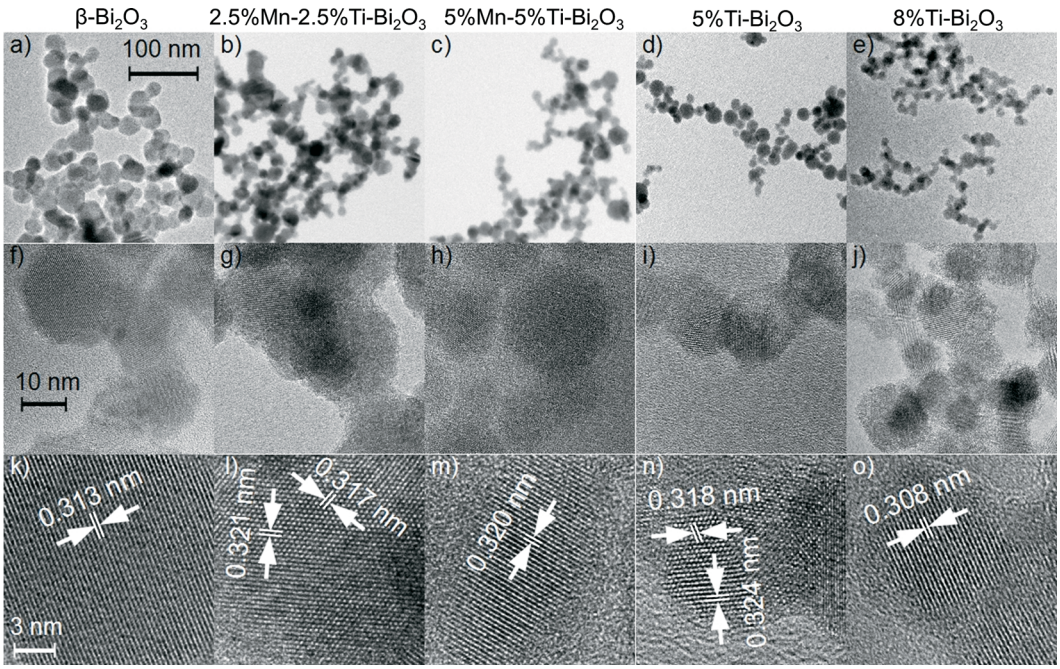

Fig. 3 Low-resolution bright field images, high-resolution images and the corresponding lattice spacing, respectively of (a, f, k) pristine β-Bi_2O_3, (b, g, l) 2.5%Ti–2.5%Mn–Bi_2O_3, (c, h, m) 5%Ti–5%Mn–Bi_2O_3, (d, i, n) 5%Ti–Bi_2O_3 and (e, j, o) 8%Ti–Bi_2O_3 nanoparticles.

arrangement can be visualized by superimposing the β-Bi_2O_3 structure parallel to [110] and the δ-Bi_2O_3 structure in the [111] direction on high-resolution TEM images with only the metal atoms shown as high-density centers (Fig. 4a and b, respectively). Further analyzing the O atom arrangement reveals that each of the 8*c* sites is evenly surrounded by four of the 32*f* sites (Fig. 4c and d). Due to the physical constraints (ionic radius of O^{2-} is 1.35 to 1.4 Å depending on its coordination),[29] only one site within each c*f*-cluster (*i.e.*, one central *c* enclosed by four *f*-positions) can be occupied by oxygen. However, the additional 32*f* positions significantly reduce the required hopping distance between adjacent *cf*-clusters (Fig. 5). For the $Fm\bar{3}m$ structure with exclusive 8*c* Wyckoff positions only $c \rightarrow c$ transitions with a hopping distance of 2.75 Å would be possible. Notably, some *ab initio* and oxygen diffusion simulations were based on such simplified structures,[36] possibly leading to inaccuracies. In contrast, $c \rightarrow f/f \rightarrow c$ transitions within one *cf*-cluster only require overcoming 0.71 Å and the $f \rightarrow f$ hopping distance between adjacent *cf*-clusters is only 1.94 Å (Fig. 5). As the oxygen ion mobility in solid oxides is based on the hopping of O to adjacent vacant sites,[7,8] this reduced distance could perhaps explain the energetically favorable oxygen transport path that gives rise to the excellent oxygen conductivity reported for δ-Bi_2O_3.[5] A recent first-principles molecular dynamics study confirmed the importance of the 32*f* sites and led to excellent agreement between calculated and measured oxygen conductivities.[8] In contrast to δ-Bi_2O_3, the distance between two neighboring oxygen positions in β-Bi_2O_3 is >2.44 Å. Thus, even if oxygen vacancies would be present in the β-Bi_2O_3, *e.g.* by removing oxygen from the particle surface through H_2 reduction or ultra-high vacuum (see below), the oxygen ion mobility in the β-phase is expected to be significantly lower than that in the δ-phase.

Metal oxidation states and optical properties

XPS analysis was applied to investigate the metal oxidation states and hence gain information on the number of oxygen vacancies in the flame-made δ-Bi_2O_3. A peak deconvolution of the Bi 4f signal in Fig. 6a revealed the typical Bi^{3+} in Bi_2O_3 (peak binding energies: Bi $4f_{5/2}$ 158.3 eV, and Bi $4f_{7/2}$ 163.6 eV).[37,38]

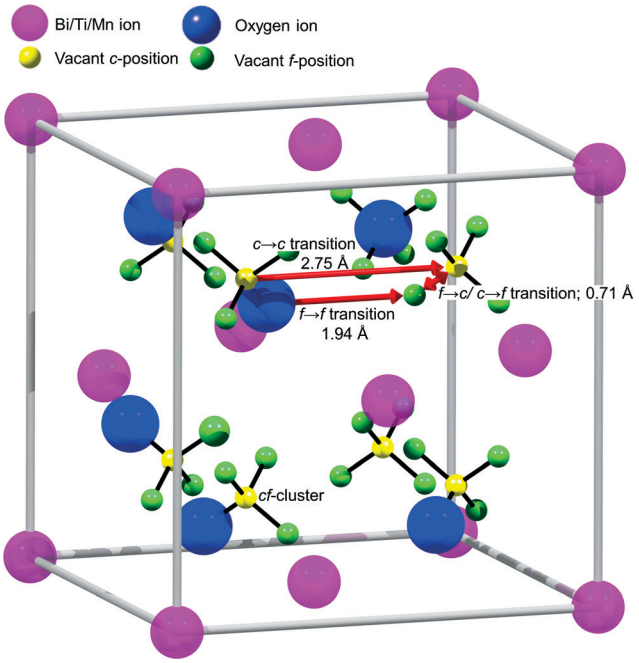

Fig. 5 Scheme of the proposed oxygen transport mechanism in δ-Bi_2O_3. The additional 32*f* Wyckoff positions reduce the hopping distance between adjacent *cf*-clusters by 30%.

Additional peaks at 159.3 and 164.6 eV were measured, which can be attributed to either Bi^{3+} in $Bi_2O_2CO_3$ (ref. 39) or that adjacent to oxygen vacancies.[40] Bi_2O_3 is prone to forming carbonate on the surface when exposed to CO_2 such as that in air[41] or from the combustion process in FSP. Nevertheless, the bulk content of the carbonate species in the present study is negligibly small and below the detection limits of the XRD and HRTEM. The peak deconvolutions of the O 1s core levels (Fig. 6c) show the lattice O^{2-} in Bi_2O_3 (peak binding energy 529.2 eV) and a broad shoulder centered ~530.9 eV belonging to the surface adsorbed O_2 and hydroxyl/carbonate species.[37,39] Note that in the case of high Mn-doping (10 at% Mn), an additional peak centered at 259.8 eV was required to fit the relatively broad O 1s spectra. The peak can be traced to the O^{2-} of MnO,[42] indicating the formation

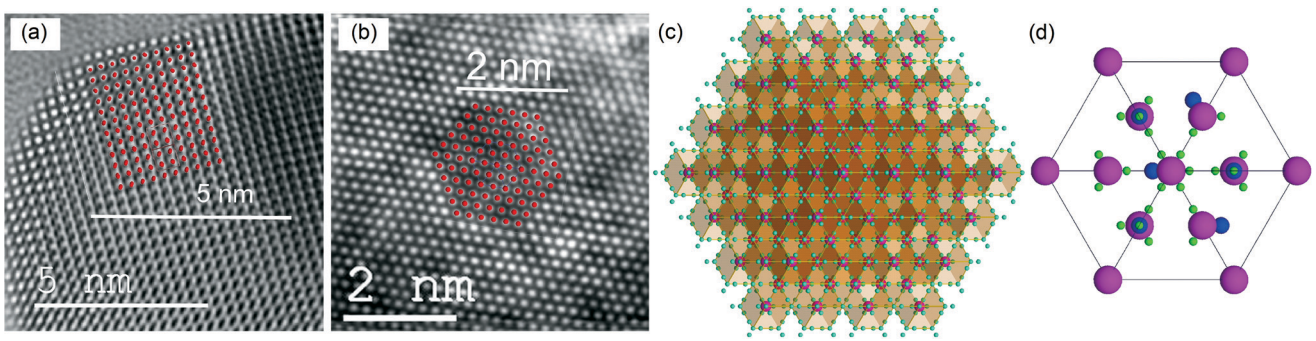

Fig. 4 High-resolution TEM images (bottom scale bars) of (a) β-Bi_2O_3 and (b) 5%Ti–Bi_2O_3 with superimposed Bi atoms in β-Bi_2O_3 in the [110] direction (with 10% scaling) and δ-Bi_2O_3 in the [111] projection (top scale bars). (c) δ-Bi_2O_3 crystal structure in the [111] direction with partially occupied oxygen positions (small greenish-blue spheres) and fully occupied mixed Bi/Ti/Mn positions (large magenta spheres). (d) One enlarged unit cell with a specific arrangement of six occupied oxygen positions (middle sized blue spheres), 32 vacancies (small green spheres) and the fully occupied Bi/Ti/Mn positions (large magenta spheres).

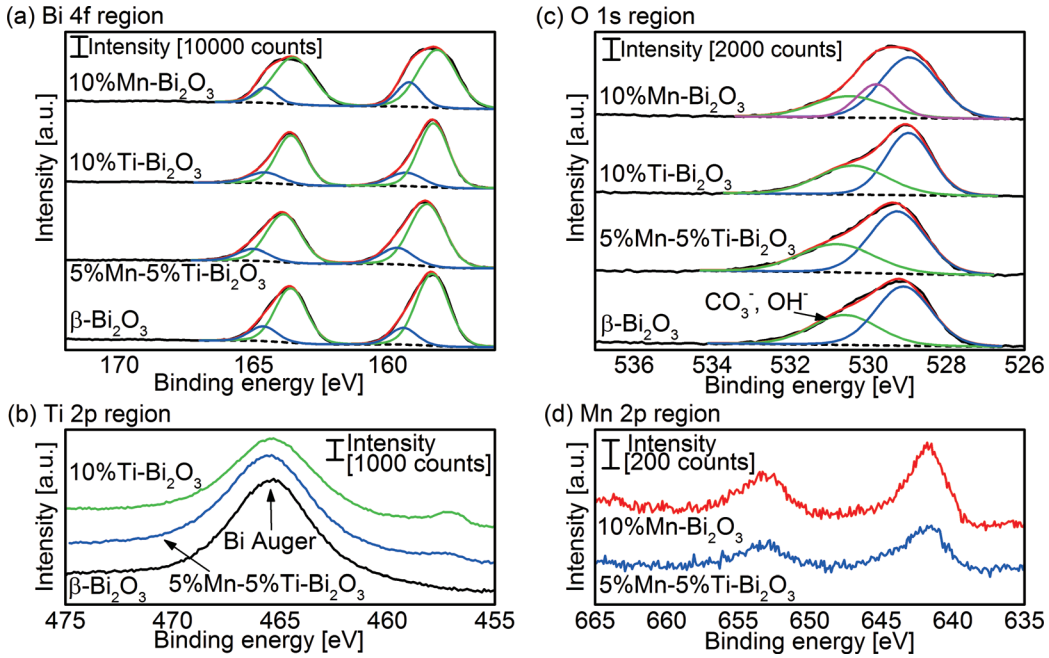

Fig. 6 XPS peak deconvolution of the (a) Bi 4f, (b) Ti 2p and (c) O 1s regions of as-prepared pristine Bi_2O_3 and that doped with Mn and/or Ti. Also shown is (d) the Mn 2p region of 10%Mn–Bi_2O_3 and 5%Mn–5%Ti–Bi_2O_3.

of MnO_x clusters and/or its segregation on the surface. Quantification of the surface elements found the Mn/Bi atomic ratio of 0.052 for the 5%Mn–5%Ti–Bi_2O_3 and 0.075 for 10%Mn–Bi_2O_3 compared to the nominal bulk values of 0.053 and 0.110, respectively. In other words, the clustering of MnO_x (instead of homogeneous dispersion of the dopant) may have taken place at high Mn concentration. Fig. 6d shows the Mn $2p_{3/2}$ spectra of the doped Bi_2O_3 with peak binding energies centered at 641.6 eV. Attempting to determine the valencies of the Mn dopant is rather challenging given the close proximity of Mn^{2+} (binding energy 640.9–641.60 eV) and Mn^{3+} (binding energy 641.32–641.9 eV).[42,43] Instead, the Mn oxidation state was determined with electron energy loss spectroscopy (EELS; Fig. S1†). A Mn $L_{2,3}$ ratio of 3.7 ± 0.3 was calculated for both the 2.5%Mn–2.5%Ti–Bi_2O_3 and the 5%Mn–5%Ti–Bi_2O_3 samples, inferring the presence of Mn^{2+}.[44] The Ti $2p_{3/2}$ peak binding energy at 457 eV is in agreement with reported values of Ti^{4+} in bismuth titanates (Fig. 6b).[40] From these results, it is deduced that the Mn and Ti dopants in Bi_2O_3 exist in the +2 and +4 states, respectively. Therefore, the general formula of the Mn/Ti stabilized δ-Bi_2O_3 is $Bi^{3+}_{2-x-y}Ti^{4+}_{x}Mn^{2+}_{y}O_{3+x/2-y/2}$. Introducing both dopants equimolarly preserves the net valency of the host matrix (*i.e.*, Bi^{3+}).

The optical bandgaps of the Bi_2O_3 samples were obtained with UV/vis diffuse-reflectance measurements (Fig. 7). Pristine

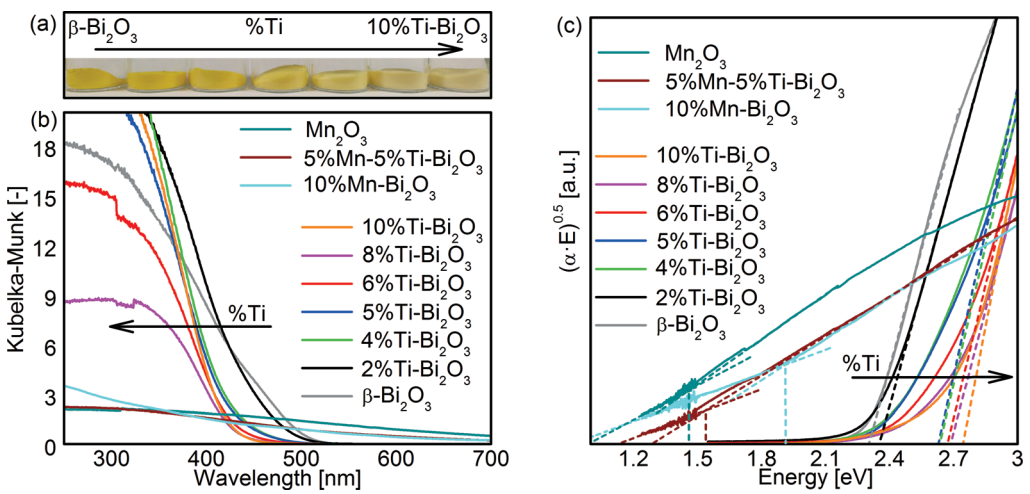

Fig. 7 (a) Photograph of as-prepared pristine Bi_2O_3 powder and that gradually doped with 2, 4, 5, 6, 8 and 10 at% Ti and (b) the corresponding UV-vis absorbance of the powders measured in Kubelka–Munk (KM) function. The KM absorbance of as-prepared Mn_2O_3, 5%Mn–5%Ti–Bi_2O_3 and 10%Mn–Bi_2O_3 is also included. (c) The Tauc plot of all the powder samples for estimation of optical bandgap, assuming allowed indirect transition.

β-Bi_2O_3 is defined by a bandgap value (E_g) of 2.3 eV as deduced from the Tauc plot (Fig. 7c and Table 1) assuming an allowed indirect electron transition, consistent with the reported values (2.1–2.6 eV).[31,45] Doping of Ti from 0 to 10 at% resulted in a gradual blueshift (see color change in Fig. 7a) in the bandgap from 2.3 to 2.8 eV, respectively. This can be attributed in part to the transformation of β- to δ-Bi_2O_3 (2.79 eV for indirect and 3.1 eV for direct electron transitions).[46] For the Mn-containing samples, the measured absorption thresholds of 1.6 eV for 5%Mn–5%Ti–Bi_2O_3 and 1.9 eV for 10%Mn–Bi_2O_3 are likely to be dominated by the *d–d* transition of MnO_x species[47] and hence prevented the meaningful extraction of bandgap values of the doped Bi_2O_3. Nevertheless, the clustering of MnO_x corroborates the earlier observations by XRD (Fig. 2d) and XPS (Fig. 6).

Thermal stability of δ-Bi_2O_3

To assess the thermal stability of the as prepared δ-Bi_2O_3, high temperature XRD (HT-XRD) measurements were carried out. As shown in Fig. 8a, the δ-Bi_2O_3 phase with 10 at% Ti was effectively preserved up to 325 °C, above which additional diffraction peaks at 31.5° and 54° 2θ emerged, indicating β-Bi_2O_3. Rietveld refinement of the XRD pattern (at 30 °C) after completion of the HT-XRD scanning up to 650 °C (R_p = 4.5%, $R_{p'}$ = 17.8%, Fig. 8b) suggested the formation of 84.5 ± 1.4% $Bi_{12}TiO_{20}$ (R_{Bragg} = 5.0%, PDF 34-0097)[48] along with 15.5 ± 0.4% $Bi_4Ti_3O_{12}$ (R_{Bragg} = 17.1%, PDF 01-089-7501).[49] Prolonged heat treatment at 300 °C for up to 79 h did not show any transformation of the 10%Ti–Bi_2O_3, highlighting its long-term stability (Fig. 8c). Doping with 10 at% Mn slightly enhanced the stability up to 350 °C, above which β-Bi_2O_3 started forming (Fig. 8d). Similar to the 10%Ti–Bi_2O_3 sample, the phase transformation was irreversible and predominantly $Bi_{12}MnO_{20}$ was formed at 650 °C (PDF 01-082-1024).

The equimolar co-doping of Mn and Ti with 5 at% each further increased the temperature stability of the δ-phase to 400 °C (Fig. 8e). This reaffirms the hypothesis that the minimization of aliovalency through co-doping of Ti^{4+} and Mn^{2+} increases the thermal stability of the metastable δ-Bi_2O_3

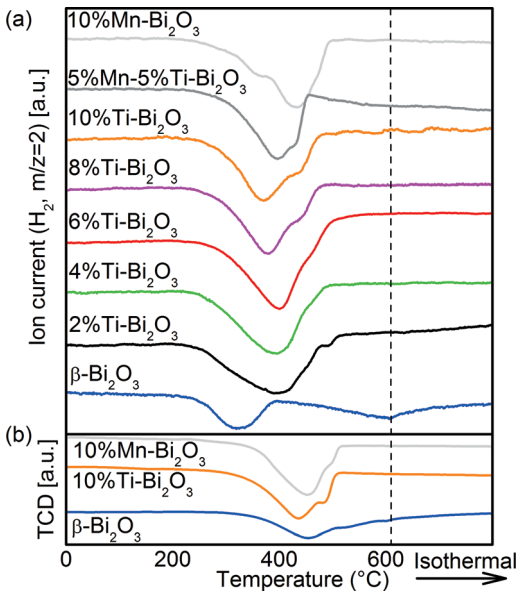

Fig. 9 H_2-TPR spectra of the pristine and doped Bi_2O_3 samples synthesized with FSP: (a) as-synthesized samples and (b) after a 1 h Ar pretreatment at 450 °C.

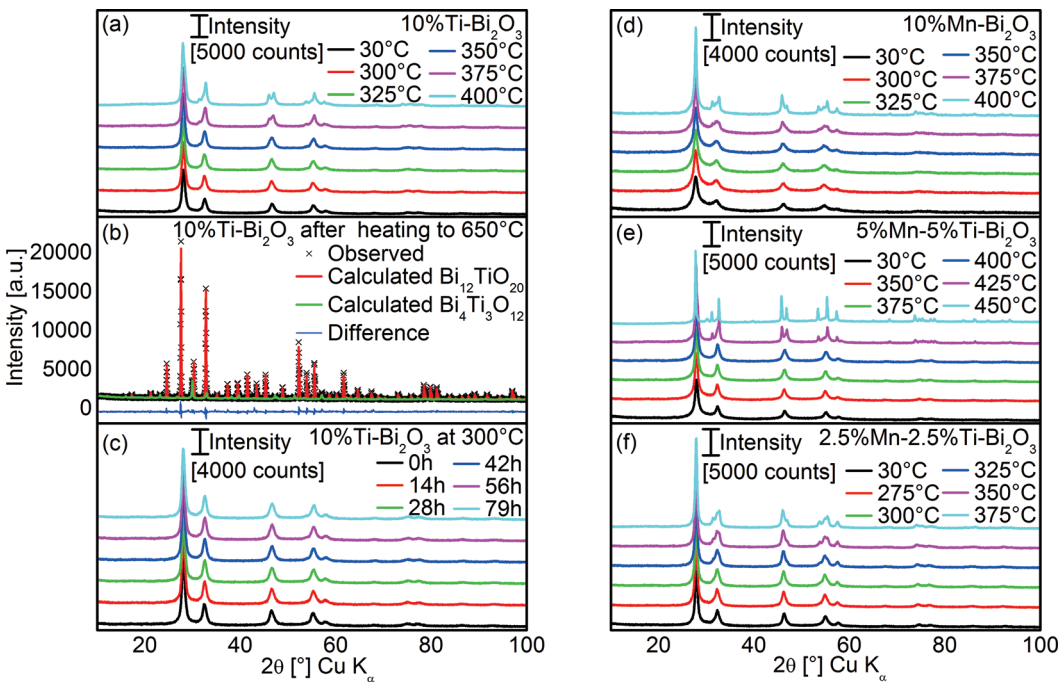

Fig. 8 (a) HT-XRD patterns of 10%Ti–Bi_2O_3 measured as a function of heating temperature and (b) corresponding Rietveld refinement fit of the sample at 30 °C after HT-XRD of up to 650 °C. (c) The HT-XRD patterns of 10%Ti–Bi_2O_3 measured at 300 °C as a function of heating time. Also shown are the HT-XRD patterns of (d) 10%Mn–Bi_2O_3, (e) 5%Mn–5%Ti–Bi_2O_3 and (f) 2.5%Mn–2.5%Ti–Bi_2O_3 measured as a function of heating temperature.

phase. Sufficient amounts of co-dopants are, however, required to preserve the δ-phase at higher temperatures which is illustrated by the reduced stability with lower amounts of equimolar Mn and Ti of 2.5 at% (Fig. 8f).

Temperature-programmed reduction with H_2 (H_2-TPR) was carried out to quantify the oxygen removal from (and mobility in) the Bi_2O_3 samples. As shown in Fig. 9a, the first surface reduction hump of pristine β-Bi_2O_3 is centered at 322 °C,[50] equivalent to 2.3 mmol g^{-1} H_2 consumed. This corresponds to 36% of the oxygen available in the sample as 6.4 mmol g^{-1} H_2 would be required for the complete reduction of Bi_2O_3. More specifically, the reduction corresponds to the outer 1.4 nm shell of the 20 nm β-Bi_2O_3 particles. Thus oxygen from the β-Bi_2O_3 surface is removed easily but due to the limited oxygen mobility within the bulk, the removed oxygen is not replenished. This is most likely linked to the comparably large distance between adjacent oxygen positions of >2.44 Å and the lack of bulk oxygen vacancies as discussed above. At higher reduction temperatures, the broad reduction of the β-Bi_2O_3 bulk between 400 and 600 °C accounts for a further 3.0 mmol g^{-1} H_2 consumption, and thus 83% of the available oxygen was consumed below 600 °C. Doping with 2 at% Ti resulted in the merging of surface and bulk reduction (6.8 mmol g^{-1}) with a peak maximum at 400 °C and a minor peak at 488 °C (0.1 mmol g^{-1}). The significant increase in H_2 consumption is a result of enhanced oxygen mobility and indicates continuous replenishment of the consumed surface oxygen. With further increase in Ti content, the bulk Bi_2O_3 reduction peak shifts towards lower temperatures (from 400 °C for 2%Ti–Bi_2O_3 to 372 °C for 10%Ti–Bi_2O_3) inferring an increase in oxygen mobility. The addition of 10 at% Mn resulted in a distinct surface reduction at 369 °C and a bulk reduction peak at 433 °C. Again, approximately 100% of the available oxygen was consumed (6.7 mmol g^{-1}), demonstrating the enhanced oxygen mobility compared to partially reducible β-Bi_2O_3. The ease in replenishing the removed surface oxygen in δ-Bi_2O_3 is hereby associated to the low transition distance between adjacent *cf*-clusters of 1.94 Å due to the 32*f* Wyckoff positions in the $Fm\bar{3}m$ crystal structure (Fig. 5). Minor CO_2 desorption was detected for all samples

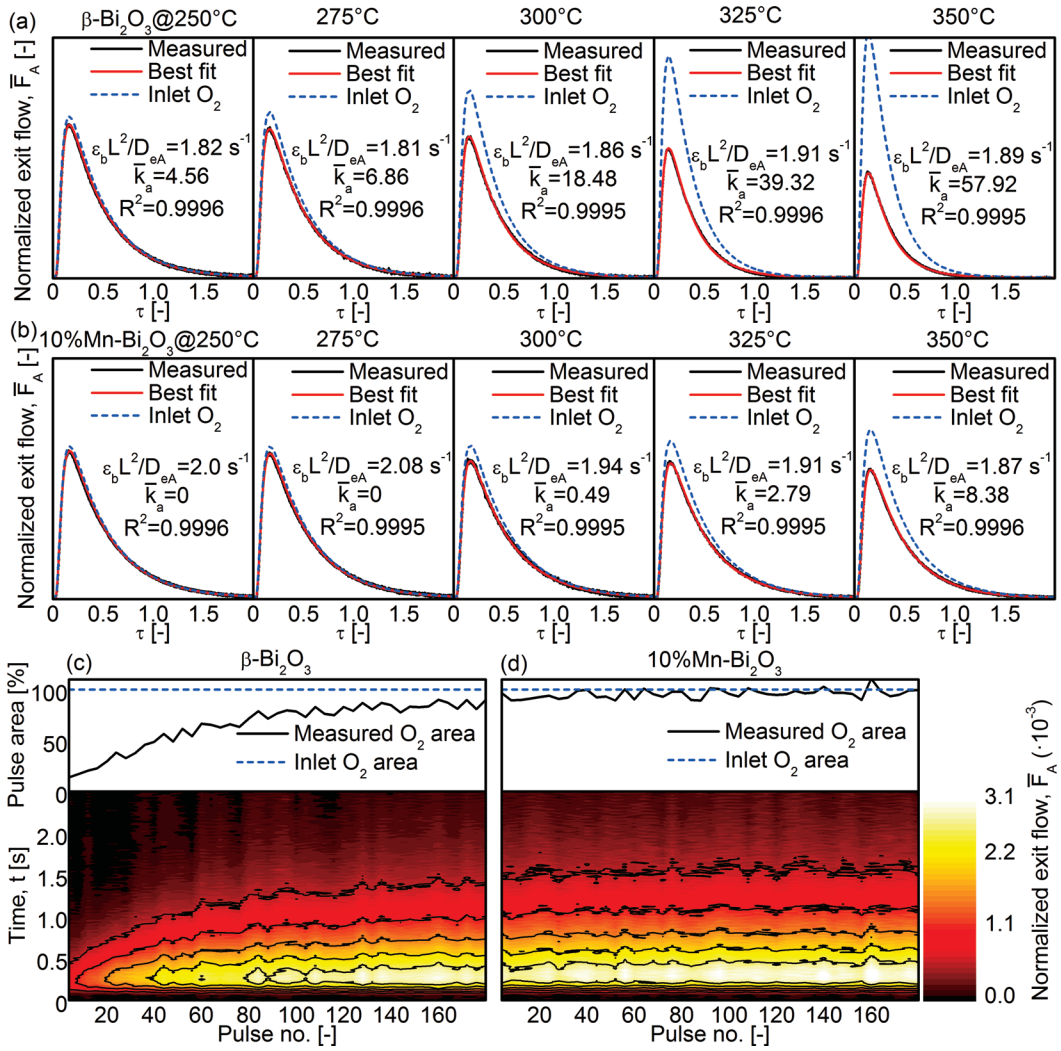

Fig. 10 TAP-2 isotopic $^{18}O_2$ pulse shape at 250–350 °C for the (a) β-Bi_2O_3 and (b) 10%Mn–Bi_2O_3 samples. Also shown are the measured $^{18}O_2$ peak area (top) and the corresponding contour plots of the $^{18}O_2$ peaks (bottom) for the (c) β-Bi_2O_3 and (d) 10%Mn–Bi_2O_3 samples at 350 °C.

during the H_2-TPRs (Fig. S2†), corroborating the formation of small amounts of surface carbonates seen earlier from XPS (Fig. 6a). Further H_2-TPRs were conducted after a 1 h Ar pretreatment at 450 °C (Fig. 9b) to alter the crystal structure while leaving the chemical composition unchanged (Fig. 8). The temperatures required for surface reduction increased from 230 °C to 280 °C after the Ar pretreatment and also the peak temperature increased (*e.g.*, 370 °C to 440 °C for 10%Ti–Bi_2O_3). Hence, the enhanced oxygen mobility in Fig. 9a is caused by the δ-phase and not simply the chemical composition of the samples (*i.e.*, the addition of Ti and/or Mn).

To study the ability of the Bi_2O_3 for heterogeneous oxygen exchange, temporal analysis of products (TAP) was conducted using gas pulses consisting of 66.7% $^{18}O_2$ isotope in Ar (Fig. 10). The average of 20 pulses was fitted to the analytical equations (see Experimental section) to determine the dimensionless adsorption and desorption rate constants ($\bar{k}_a$ and $\bar{k}_d$, respectively) and the effective Knudsen diffusivity of oxygen (D_{eA}). As shown in Fig. 10a, the $\bar{k}_a$ of pristine β-Bi_2O_3 increased from 4.6 at 250 °C to 57.9 at 350 °C while $\bar{k}_d$ remained 0. A release of ^{16}O (*i.e.*, $^{16}O^{18}O$ or $^{16}O_2$; not shown) was not detected and the $^{18}O_2$ peak area increased with increasing number of pulses (Fig. 10c). Given the low-temperature reducibility of β-Bi_2O_3 (Fig. 9a), some of the surface may have been reduced under the ultra-high vacuum and elevated temperatures, and this accounts for the consumption of $^{18}O_2$ during TAP measurements (Fig. 10c, top). Essentially, the $^{18}O_2$ peak areas converge towards that of the Inlet O_2 area (corresponding to 100% O_2 exiting the reactor; see Experimental section) as the vacancy sites are fully saturated (Fig. 10c, top). Because 10%Mn–Bi_2O_3 is less reducible at low temperatures (despite the overall higher reducibility at high temperatures) the difference between measured and expected O_2 area (compare Measured and Inlet O_2 in Fig. 10a) is much smaller for 10%Mn–Bi_2O_3 than for β-Bi_2O_3. No ^{16}O release was detected and $\bar{k}_d$ remained 0 in the whole temperature range. From the measurements, it is concluded that the cationic doping in Bi_2O_3 stabilized not only the δ-phase with its numerous oxygen vacancies but also the surface lattice oxygen in Bi_2O_3. Such stabilization of lattice oxygen is in agreement with the decrease in heterogeneous oxygen exchange with increasing cation concentrations reported in the literature.[6,9,16,51] It is believed that this can be overcome by introducing co-catalysts such as Pt on the surface of δ-Bi_2O_3 to assist in the dissociative adsorption of molecular O_2 and further its interfacial exchange. In that way, the beneficial effect of O mobility (as reflected by its bulk reducibility) can be fully exploited.

Conclusions

Flame spray pyrolysis (FSP) is a technique for effectively stabilizing nano-sized δ-Bi_2O_3 down to room temperature with remarkably low dopant concentrations. This extraordinarily low cation concentration is expected to be beneficial for the oxygen ion conductivity. Extensive characterization revealed that 5 at% (2.5% Mn + 2.5% Ti) was sufficient for almost pure δ-phase nanoparticles, while 10 at% Ti, 10 at% Mn as well as 5 at% Mn + 5 at% Ti all resulted in pure δ-Bi_2O_3. Adding a mixture of two cations (*i.e.*, Ti and Mn) during FSP hereby lowered the required amount for δ-Bi_2O_3 stabilization and caused an increase in thermal stability. H_2 temperature programmed reduction and temporal analysis of products indicated enhanced bulk oxygen mobility for the as-synthesized δ-Bi_2O_3 while β-Bi_2O_3 was superior in surface reducibility. In the present study, materials are already applicable at a temperature range of 100–325 °C and further optimization by, *e.g.*, different cation combinations depending on the desired applications, is feasible. The single-step synthesis and versatility of the FSP technique is expected to set the foundation for the development of novel bismuth-based solid oxygen conductors.

Acknowledgements

JAHD thanks the support of the Research Grant Council (RGC) of Hong Kong for awarding the Hong Kong PhD Fellowship Scheme. The work is supported by the RGC through the General Research Fund (Project 11302714). MGH and AU thank MINECO for support through Severo Ochoa Excellence Accreditation 2014-2018 (SEV-2013-0319). SP and LM gratefully acknowledge the financial support of the Deutsch Forschungsgemeinschaft (DFG) within the SPP 1613 (MA 3333/6-1) and the Priority Program "Partikel im Kontakt -Mikromechanik, Mikroprozessdynamik und Partikelkollektiv" (SPP 1486) under grants MA 3333/3."

References

1 M. Yan, F. Chen, J. Zhang and M. Anpo, *J. Phys. Chem. B*, 2005, **109**, 8673–8678.
2 Y. K. Kho, W. Y. Teoh, L. Mädler and R. Amal, *Chem. Eng. Sci.*, 2011, **66**, 2409–2416.
3 (*a*) J. H. Shim, C.-C. Chao, H. Huang and F. B. Prinz, *Chem. Mater.*, 2007, **19**, 3850–3854; (*b*) S. Sanna, V. Esposito, A. Tebano, S. Licoccia, E. Traversa and G. Balestrino, *Small*, 2010, **6**, 1863–1867.
4 (*a*) L. Malavasi, C. A. J. Fisher and M. S. Islam, *Chem. Soc. Rev.*, 2010, **39**, 4370–4387; (*b*) A. Orera and P. R. Slater, *Chem. Mater.*, 2010, **22**, 675–690.
5 (*a*) E. D. Wachsman and K. T. Lee, *Science*, 2011, **334**, 935–939; (*b*) R. Punn, A. M. Feteira, D. C. Sinclair and C. Greaves, *J. Am. Chem. Soc.*, 2006, **128**, 15386–15387.
6 M. Drache, P. Roussel and J.-P. Wignacourt, *Chem. Rev.*, 2007, **107**, 80–96.
7 (*a*) R. Pornprasertsuk, P. Ramanarayanan, C. B. Musgrave and F. B. Prinz, *J. Appl. Phys.*, 2005, **98**, 103513; (*b*) P. S. Manning, J. D. Sirman, R. A. De Souza and J. A. Kilner, *Solid State Ionics*, 1997, **100**, 1–10.
8 A. Seko, Y. Koyama, A. Matsumoto and I. Tanaka, *J. Phys.: Condens. Matter*, 2012, **24**, 475402.
9 J. C. Boivin and G. Mairesse, *Chem. Mater.*, 1998, **10**, 2870–2888.
10 J. A. Switzer, M. G. Shumsky and E. W. Bohannan, *Science*, 1999, **284**, 293–296.

11 H. A. Harwig, *Z. Anorg. Allg. Chem.*, 1978, **444**, 151–166.
12 (*a*) A. Helfen, S. Merkourakis, G. Wang, M. G. Walls, E. Roy, K. Yu-Zhang and Y. Leprince-Wang, *Solid State Ionics*, 2005, **176**, 629–633; (*b*) K. Laurent, G. Y. Wang, S. Tusseau-Nenez and Y. Leprince-Wang, *Solid State Ionics*, 2008, **178**, 1735–1739.
13 H. T. Fan, S. S. Pan, X. M. Teng, C. Ye and G. H. Li, *J. Phys. D: Appl. Phys.*, 2006, **39**, 1939–1943.
14 T. Takeyama, N. Takahashi, T. Nakamura and S. Itoh, *J. Cryst. Growth*, 2005, **275**, 460–466.
15 X. Y. Chen, Z. J. Zhang and S. W. Lee, *J. Solid State Chem.*, 2008, **181**, 166–174.
16 D. W. Jung, K. L. Duncan and E. D. Wachsman, *Acta Mater.*, 2010, **58**, 355–363.
17 K. T. Lee, A. A. Lidie, H. S. Yoon and E. D. Wachsman, *Angew. Chem., Int. Ed.*, 2014, **53**, 13463–13467.
18 S. Sanna, V. Esposito, J. W. Andreasen, J. Hjelm, W. Zhang, T. Kasama, S. B. Simonsen, M. Christensen, S. Linderoth and N. Pryds, *Nat. Mater.*, 2015, **14**, 500–504.
19 A. J. Jacobson, *Chem. Mater.*, 2010, **22**, 660–674.
20 G. Meng, C. Chen, X. Han, P. Yang and D. Peng, *Solid State Ionics*, 1988, **28–30**, 533–538.
21 A. Watanabe, M. Drache, J. P. Wignacourt, P. Conflant and J. C. Boivin, *Solid State Ionics*, 1993, **67**, 25–28.
22 (*a*) S. Pokhrel, A. E. Nel and L. Mädler, *Acc. Chem. Res.*, 2013, **46**, 632–641; (*b*) S. Pokhrel, J. Birkenstock, M. Schowalter, A. Rosenauer and L. Mädler, *Cryst. Growth Des.*, 2010, **10**, 632–639; (*c*) J. A. Kemmler, S. Pokhrel, L. Mädler, U. Weimar and N. Barsan, *Nanotechnology*, 2013, **24**, 442001; (*d*) W. Y. Teoh, R. Amal and L. Mädler, *Nanoscale*, 2010, **2**, 1324–1347; (*e*) R. Strobel and S. E. Pratsinis, *J. Mater. Chem.*, 2007, **17**, 4743–4756.
23 (*a*) J. A. Kemmler, S. Pokhrel, J. Birkenstock, M. Schowalter, A. Rosenauer, N. Bârsan, U. Weimar and L. Mädler, *Sens. Actuators, B*, 2012, **161**, 740–747; (*b*) J. Xiao, A. Kuc, S. Pokhrel, M. Schowalter, S. Parlapalli, A. Rosenauer, T. Frauenheim, L. Mädler, L. G. M. Pettersson and T. Heine, *Small*, 2011, **7**, 2879–2886; (*c*) J. Xiao, A. Kuc, S. Pokhrel, L. Mädler, R. Pöttgen, F. Winter, T. Frauenheim and T. Heine, *Chem. – Eur. J.*, 2013, **19**, 3287–3291.
24 L. Mädler, H. K. Kammler, R. Mueller and S. E. Pratsinis, *J. Aerosol Sci.*, 2002, **33**, 369–389.
25 L. Cavé, T. Al, D. Loomer, S. Cogswell and L. Weaver, *Micron*, 2006, **37**, 301–309.
26 J. T. Gleaves, G. S. Yablonskii, P. Phanawadee and Y. Schuurman, *Appl. Catal., A*, 1997, **160**, 55–88.
27 L. Mädler and S. E. Pratsinis, *J. Am. Ceram. Soc.*, 2002, **85**, 1713–1718.
28 S. E. Pratsinis, *Prog. Energy Combust. Sci.*, 1998, **24**, 197–219.
29 R. D. Shannon, *Acta Crystallogr., Sect. A: Cryst. Phys., Diffr., Theor. Gen. Crystallogr.*, 1976, **32**, 751–767.
30 D. Poleti, L. Karanović, M. Zdujić and C. Jovalekić, *J. Serb. Chem. Soc.*, 2012, **77**, 1091–1096.
31 Y. Wang, Y. Wen, H. Ding and Y. Shan, *J. Mater. Sci.*, 2010, **45**, 1385–1392.
32 H. Kato and A. Kudo, *J. Phys. Chem. B*, 2002, **106**, 5029–5034.
33 A. A. Zav'yalova and R. M. Imamov, *J. Struct. Chem.*, 1973, **13**, 811–814.
34 F. Hund, *Z. Anorg. Allg. Chem.*, 1964, **333**, 248–255.
35 M. Yashima and D. Ishimura, *Chem. Phys. Lett.*, 2003, **378**, 395–399.
36 (*a*) G. Zhong, Y. Wang, Z. Dai, J. Wang and Z. Zeng, *Phys. Status Solidi B*, 2009, **246**, 97–101; (*b*) G. Zhong, J. Wang and Z. Zeng, *Phys. Status Solidi B*, 2008, **245**, 2737–2742.
37 (*a*) D. Barreca, F. Morazzoni, G. A. Rizzi, R. Scotti and E. Tondello, *Phys. Chem. Chem. Phys.*, 2001, **3**, 1743–1749; (*b*) H. Cheng, B. Huang, J. Lu, Z. Wang, B. Xu, X. Qin, X. Zhang and Y. Dai, *Phys. Chem. Chem. Phys.*, 2010, **12**, 15468–15475.
38 M. Liu, L. Zhang, K. Wang and Z. Zheng, *CrystEngComm*, 2011, **13**, 5460–5466.
39 Q. Li, H. Liu, F. Dong and M. Fu, *J. Colloid Interface Sci.*, 2013, **408**, 33–42.
40 C. Zaldo, C. Coya, J. L. G. Fierro, K. Polgár, L. Kovács and Z. Szaller, *J. Phys. Chem. Solids*, 1996, **57**, 1667–1672.
41 (*a*) I. Djerdj, A. Haensch, D. Koziej, S. Pokhrel, N. Barsan, U. Weimar and M. Niederberger, *Chem. Mater.*, 2009, **21**, 5375–5381; (*b*) L. Huang, G. Li, T. Yan, J. Zheng and L. Li, *New J. Chem.*, 2011, **35**, 197–203.
42 (*a*) A. A. Audi and P. M. A. Sherwood, *Surf. Interface Anal.*, 2002, **3**, 274–282; (*b*) J. S. Foord, R. B. Jackman and G. C. Allen, *Philos. Mag. A*, 1984, **49**, 657–663.
43 A. S. Ivanova, E. M. Slavinskaya, V. V. Mokrinskii, I. A. Polukhina, S. V. Tsybulya, I. P. Prosvirin, V. I. Bukhtiyarov, V. A. Rogov, V. I. Zaikovskii and A. S. Noskov, *J. Catal.*, 2004, **221**, 213–224.
44 H. K. Schmid and W. Mader, *Micron*, 2006, **37**, 426–432.
45 V. Dolocan and F. Iova, *Phys. Status Solidi A*, 1981, **64**, 755–759.
46 (*a*) L. Zhou, W. Wang, H. Xu, S. Sun and M. Shang, *Chem. – Eur. J.*, 2009, **15**, 1776–1782; (*b*) H. A. Zayed, *Fizika (Alma-Ata)*, 1995, **4**, 45–53.
47 (*a*) M. Tepluchin, D. K. Pham, M. Casapu, L. Mädler, S. Kureti and J.-D. Grunwaldt, *Catal. Sci. Technol.*, 2015, **5**, 455–464; (*b*) N. Stamatis, K. Goundani, J. Vakros, K. Bourikas and C. Kordulis, *Appl. Catal., A*, 2007, **325**, 322–327; (*c*) S. Velu, N. Shah, T. M. Jyothi and S. Sivasanker, *Microporous Mesoporous Mater.*, 1999, **33**, 61–75.
48 *NBS Monogr. 25*, PDF #34-0097, 1983, vol. 20, p. 21.
49 C. H. Hervoches and P. Lightfoot, *Chem. Mater.*, 1999, **11**, 3359–3364.
50 R. Irmawati, M. N. N. Nasriah, Y. H. Taufiq-Yap and S. B. A. Hamid, *Catal. Today*, 2004, **93–95**, 701–709.
51 A. M. Azad, S. Larose and S. A. Akbar, *J. Mater. Sci.*, 1994, **29**, 4135–4151.

